RSC Advances

ROYAL SOCIETY OF CHEMISTRY

www.rsc.org/advances

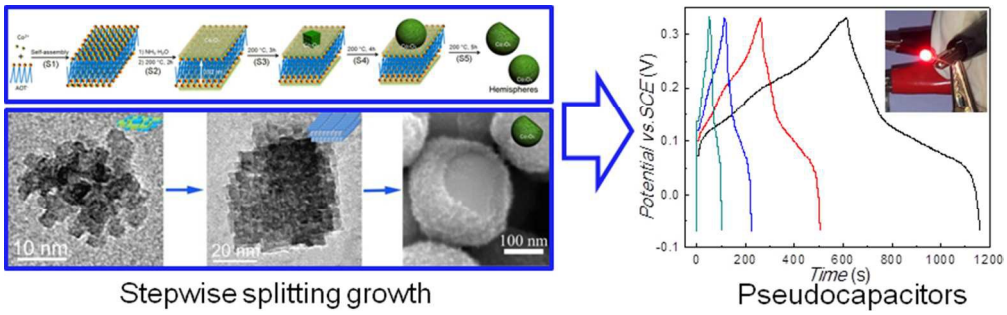

Co3O4 supercrystals for pseudocapacitors: The stepwise splitting of Co3O4 nanocuboids can generate porous and single crystalline Co3O4 hemispheres of 256.7±30.1 nm on a large scale. The Co3O4 supercrystals exhibit highly enhanced performances in storing charges.
147x45mm (150 x 150 DPI)

Cite this: DOI: 10.1039/c0xx00000x

www.rsc.org/xxxxxx

ARTICLE TYPE

Porous and single crystalline Co_3O_4 nanospheres for pseudocapacitors with enhanced performances

Yuyin Gong,[a] Feilong Gong,[a] Chaofei Wang,[a] Hegen Zheng[b] and Feng Li*[a,c]

Received (in XXX, XXX) Xth XXXXXXXXX 20XX, Accepted Xth XXXXXXXXX 20XX

DOI: 10.1039/b000000x

Porous and single-crystalline Co_3O_4 nanospheres have been synthesized successfully on a large scale. It was found that the reaction time can dramatically affect the growth of the Co_3O_4 nanospheres in nanoreactors constructed with AOT^- and Co^{2+} ions. The dynamic evolution of the nanostructures produced in the reaction strongly support a stepwise splitting mechanism proposed to understand the formation of the porous and single crystalline nanospheres. The pseudocapacitors made with the porous and single crystalline Co_3O_4 nanospheres exhibit excellent charge-storage performances. The enhanced electrochemical properties of the materials can be attributed to their superstructures with pores and single crystalline feature.

Introduction

Co_3O_4 is one of the promising materials widely applied to not only pseudocapacitors,[1] but also Li batteries,[2] sensors[3] and catalysts.[4] It has been demonstrated that the electrode materials for designing advanced energy storage devices have to facilitate both ion diffusion and electron transportation.[5] In order to improve their energy storage performances, 3D hierarchical Co_3O_4 nanoarchitectures have been investigated extensively in recent years. Among the techniques developed, topotactic transformations of Co-related precursors can keep the 3D hierarchical nanostructures and generate pores throughout the materials, after the precursors are first produced in solution and then annealed at higher temperature.[1j,1k,1m,2f-i,3,6] The porous 3D Co_3O_4 materials obtained, however, are generally composed of nanoparticles with polycrystalline feature. Only have a few cases of porous Co_3O_4 materials consisting of quasi-single crystalline nanobelts[2c,2d,7] and nanowires[2j,8] been reported and applied to Li-batteries so far. Recently, Li and co-workers found that single crystalline Co_3O_4 polyhedra can perform well in Li-storage predominated by their surface microstructures.[2b] The charge storage capabilities of most pseudocapacitors made with Co_3O_4 materials are still much lower than their theoretically specific capacitance of 3650 F g^{-1}.

Because the spherical particles could pack closely to form electrodes with high density, nanospheres with porous and single crystalline features are extremely attractive in designing and fabricating devices for energy storage and conversation. Porous and single crystalline TiO_2 nanospheres synthesized with mesoporous templates, for instance, exhibit highly enhanced energy conversation efficiency in constructing solar cells, because of substantially higher conductivity and electron mobility of the materials in comparison with their polycrystalline counter-parts.[9] It was also found that carbon materials with pores of less than 1 nm in diameter show anomalous increase in storing charges.[10] These progresses strongly suggest that there is still room for improvement in the charge storing performances of pseudocapacitors made with Co_3O_4 materials through especially optimizing their pore and skeleton structures.

The researches in our groups have been mainly focusing on building nanoarchitectures for microdevices including supercapacitors.[1i,11] Herein, we would like to report porous and single crystalline Co_3O_4 nanospheres. The pseudocapacitors made with as-prepared materials exhibit highly enhanced performances attributed to their nanostructures. The dynamic evolution of nanostructures produced in the reactions suggests a stepwise splitting mechanism for the formation of the supercrystals.

Experimental

All of the reagents were analytically pure and used as received without further purification. AOT was purchased from Aldrich-Sigma and the others from Shanghai Chemical Industrial Co. Ltd., Shanghai, China.

Synthesis of Co_3O_4 nanospheres

In a typical synthesis of Co_3O_4 nanospheres, cobalt nitrate solution was first prepared by dissolving cobalt nitrate hexahydrate ($Co(NO_3)_2 \cdot 6H_2O$) (0.7225 g, 2.50 mmol) in deionized water (90 mL) under stirring. AOT (3.3342 g, 7.50 mmol) was then dissolved in 1-butanol (10 mL) under vigorous stirring until it became transparent. Subsequently, the cobalt nitrate solution in water was added dropwise with 5 second intervals into AOT solution in 1-butanol under vigorous stirring to obtain pink colloid solution. After stirred for another 30 min at room temperature, concentrated $NH_3 \cdot H_2O$ (0.6 ml, 28wt%) was added dropwise into the mixture to obtain transparent solution with pale blue colour. The mixture was stirred for another 30 min and finally transferred into a Teflon-lined autoclave and maintained at 200 °C for 5 h. After cooled down to room temperature naturally, black precipitates were collected by centrifugation and thoroughly washed with deionized water and ethanol for 5 times each, respectively. Black powders were obtained after dried in an oven at 85 °C for 12 h.

Characterizations

The compositions of the materials were identified by powder X-ray diffraction (XRD) analysis using a D/max 2550v diffractometer with Cu Kα radiation (λ = 1.54056 Å, scan rate: 0.02° s^{-1} in the range of 5 - 80°), and thermal analysis employing a SDTQ600 thermal analyzer working at a constant heating rate of 5 °C min^{-1} in N_2. The specific surface area and pore size of the materials were measured using a Belsorp-Mini adsorption apparatus (Bel Japan Inc). The microstructures of the materials were characterized with field emission scanning electron microscopy (FESEM, JSM-7001F) and transmission electron microscopy (TEM, JEM-2100 operated at 200 kV).

Electrochemical Properties

The electrochemical studies were carried out in a three-electrode system with KOH electrolyte solution (6 mol L^{-1}). A piece of nickel mesh with as-prepared Co_3O_4 nanospheres, a platinum wire, and saturated calomel electrode (SCE) were used as working electrode, counter electrode, and reference electrode, respectively. The mixture for fabricating working electrode were composed of active Co_3O_4 materials (80 wt%), conductive material (acetylene black, ATB, 10 wt%) and binder (PTFE, 10 wt%). It was first coated onto the surfaces of nickel foam sheets (1 cm × 1 cm) and then dried at 100 °C for 12 h. The Ni sheets with electrode materials were finally pressed under 10 MPa to obtain working electrodes. The cyclic voltammograms (CV) were measured with a CHI 660D electrochemical workstation. The CV tests were done between 0 and 0.4 V (vs. saturated calomel electrode (SCE)) at scan rates of 5, 10, 20, and 50 mV s^{-1}, respectively. Galvanostatic charge/discharge cycle tests were performed on a CT2001A LAND Cell test system. The specific capacitances of the supercapacitors were evaluated from the charge/discharge tests with the following equation (Eg. 1):

$$C = I \Delta t / m \Delta V \quad (1)$$

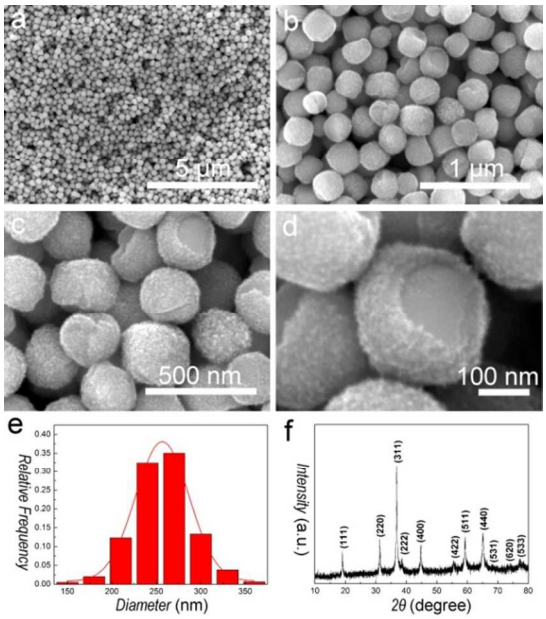

Fig. 1. a-d) FESEM images, e) size distribution and f) XRD pattern of Co_3O_4 hemispheres.

where C is the specific capacitance of the capacitor (F g^{-1}), I is the current of charge/discharge, and Δt is the discharging time period in seconds for the potential change ΔV in volts; m is the mass of the active material loaded onto the working electrode. All of the electrochemical measurements were carried out at room temperature.

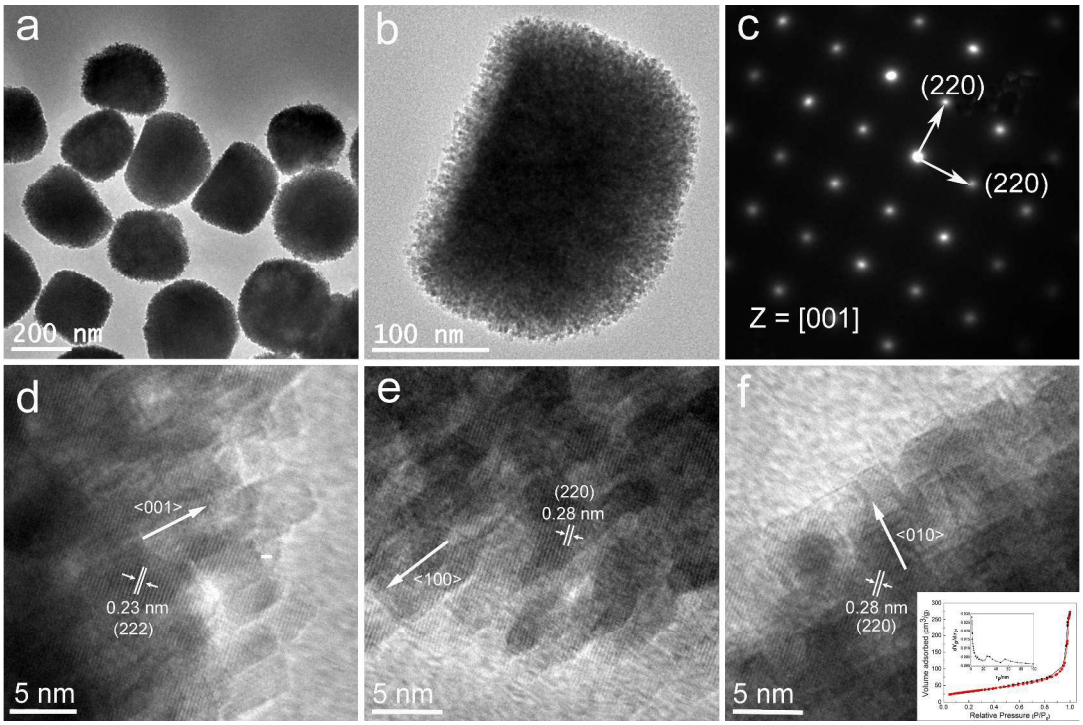

Fig. 2. a) Low magnification TEM images of Co_3O_4 hemispheres. b) TEM image and c) SAED pattern of one Co_3O_4 hemisphere. HRTEM images taken at d) bottom right, e) upper left and f) upper right areas of the nanosphere as shown in b), respectively. Inset in e): physisorption isotherms and pore-size distribution curve (inset) of Co_3O_4 hemispheres.

Results and Discussion

The as-prepared products were first characterized with field emission scanning electron microscope (FESEM) as shown in Fig. 1a-d. The low magnification FESEM image (Fig. 1a) shows that granules with high uniformity and regularity have been produced on a large scale. Fig. 1e illustrates the size distribution of the granules with diameter of 256.7±30.1 nm. The FESEM images of higher magnifications (Fig. 1b-d) of the granules reveal their surfaces covered with nanoparticles. Some of the granules also possess hemispherical geometry: one of their facets is rather flat and smooth. The XRD profile (Fig. 1f) of the materials consists of diffraction peaks corresponding to (111), (220), (311), (222), (400), (422), (511) and (440) of cubic Co_3O_4. The results are consistent well with those in JCPDS card (No. 42−1467). There is no diffraction peak from any other impurity in the XRD profile, which indicates the high purity of the products (deviation of 5%).

The Co_3O_4 nanospheres were further characterized with transmission electron microscope (TEM), high resolution transmission electron microscope (HRTEM) and selected area electron diffraction (SAED). Fig. 2a presents TEM image of Co_3O_4 nanospheres at low magnification. The TEM image (Fig. 2b) of one nanosphere at higher magnification reveals that the particles consist of nanocuboids of *ca*. 3 nm in diameter. The SAED pattern (Fig. 2c) of the whole sphere as shown in Fig. 2b is composed of well ordered dots of (220) and ($2\bar{2}0$) facets corresponding to [001] band axis, which can directly demonstrate the single crystalline nature of as-prepared Co_3O_4 granules. The HRTEM images (Fig. 2d-e) of the nanosphere performed at its upper left and bottom right areas, respectively, are composed of d-spacings of 0.28 nm attributed to (220) planes of cubic Co_3O_4. The nanocuboids grow along <100> and <010> directions, respectively, and are exposed in {100} facets. In contrast, the HRTEM image (Fig. 2f) collected at upper right area of the nanosphere is composed of d-spacings of 0.23 nm corresponding to (222) plane of cubic Co_3O_4. The results indicate that these nanocuboids orient along <001> direction and are mainly exposed in {100} planes. More details concerned with the microstructures of porous Co_3O_4 nanospheres with single crystalline nature can be further revealed by performing HRTEM (Fig. S1) around their edges. The nanocuboids as shown in Fig. 2e form relative flat and smooth facets for the hemispherical structure of the granules, compared to those in Fig. 2d and 2f. The defects resulting from the pores of 1 - 3 nm in diameter can be observed in the HRTEM images also. The inset in Fig. 2e shows the adsorption and desorption isotherm and the corresponding BJH pore size distribution plot of the Co_3O_4 nanospheres. Most of the calculated size of the pores is around 12.6 nm in diameter (pore volume: 0.35 $cm^3\ g^{-1}$). The Co_3O_4 nanospheres, which consist of nanocuboids mainly exposed in {100} facets with high BET surface area of 146.2 $m^2\ g^{-1}$, have been synthesized successfully on a large scale.

In order to understand the formation of the 3D hierarchical Co_3O_4 hemispheres, the reaction time effect on the composition and microstructure of the materials was investigated carefully. Fig. 3 shows the XRD profiles of the materials produced by varying the reaction time from 1 to 5 h. After reacting for 1 h, the materials obtained only exhibit several broaden peaks of low intensity for their low crystallinity. After prolonging the reaction to 2 h at 200 °C, however, a series of diffraction peaks, especially the strongest diffraction at 9.6° corresponding to d-spacing of 9.2 Å, appear in the XRD profile. It has been verified that the surfactant - sodium bis(2-ethylhexyl) sulfosuccinate (AOT) molecules prefer to self-assemble into lamellar structures together with metal ions, which can act as nanoreactors to confine the

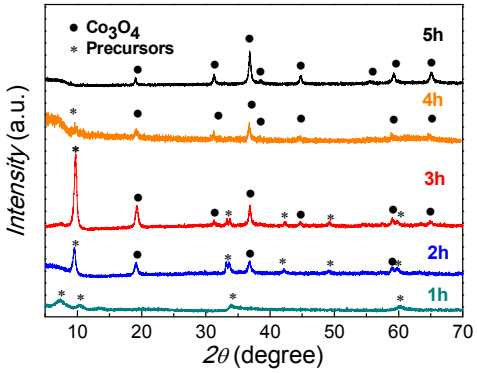

Fig. 3. The XRD profiles of the materials synthesized at 200 °C for 1, 2, 3, 4 and 5 h, respectively.

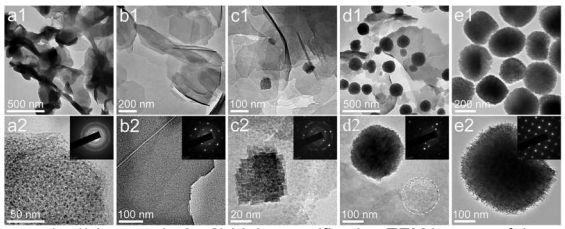

Fig. 4. a1-e1) Low and a2-e2) high magnification TEM images of the materials produced at 200 °C for 1, 2, 3, 4 and 5 h, respectively. The insets in a2-e2 are the SAED patterns of as-prepared materials.

growth of nanocrystals.[11d,11e] The hydrophobic tail of AOT can be calculated to be *ca*. 7.70 Å in length, based on the C-C bond length of 1.54 Å. The d-spacing of 9.2 Å can be therefore attributed to the lamellar assemblies formed by two layers of AOT molecules. In addition, it can be observed that the diffractions corresponding to (111) and (311) facets of cubic Co_3O_4 appear in the XRD profile of the materials after reacting at 200 °C for 2 h, which indicates that cubic Co_3O_4 has been readily generated in the reaction. The intensities of the diffractions corresponding to both Co_3O_4 and lamellar assemblies further increase and more diffraction peaks attributed to cubic Co_3O_4 appear in the XRD pattern of materials prepared by reacting for 3 h. In contrast to the intensity increase of diffractions aroused from cubic Co_3O_4, the peaks attributed to lamellar assemblies then decrease and finally disappear completely in the XRD profiles of the materials produced by performing the reactions for 4 and 5 h, respectively.

The reaction time effect on the microstructures of materials was further investigated with TEM (Fig. 4) and SEM (Fig. S2-3). After reacting at 200 °C for 1 h, 2D lamellar assemblies can be obtained as shown in Fig. 4a1-2. The SAED pattern (inset in Fig. 4a2) reveals their low crystallinity, which is consistent well with XRD profile. However, 2D nanosheets (Fig. 4b1-2) of several hundred nanometers in dimension with clear edges can be produced by reacting for 2 h. The surfaces of the 2D nanosheets (Fig. 4b1-2) are much smoother in comparison to those as shown in Fig. 4a1-2. It is interesting to found that the SAED pattern inset in Fig. 4b2 consists of well ordered dots, which indicates the single-crystalline nature of the nanosheets. After increasing the reaction time to 3 h, dendric nanocubes consisting of nanocuboids of *ca*. 9 nm in length and *ca*. 3 nm in width can be generated on the surfaces of the nanosheet (Fig. 4c1 and Fig. S2). The surfaces of the nanosheets also become ragged in accompanying with the appearance of nanocibes. After further prolonging the reaction

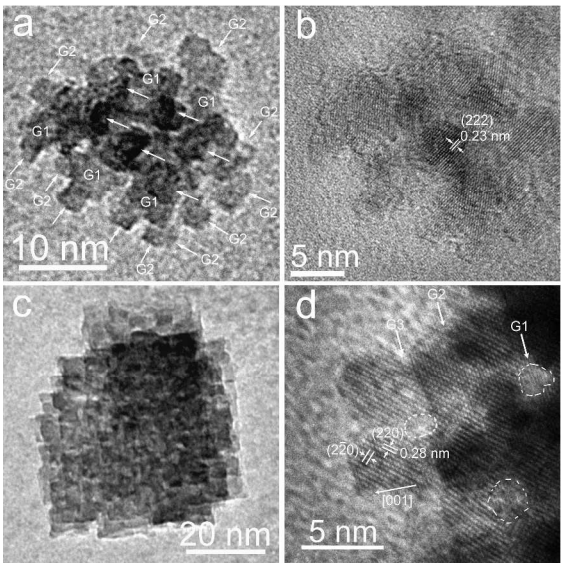

Fig. 5. a) TEM and b) HRTEM images of Co_3O_4 nanosheets after reacting for 2 h. c) TEM and d) HRTEM images of a nano-jenga after reacting for 3 h.

time to 4 h, Co_3O_4 granules of *ca*. 180 nm in diameter (Fig. 4d1-2 and Fig. S3) are generated on the surfaces of the nanosheets. Compared to the nanodisks with straight edges as shown in Fig. 4b1, the nanosheets change into irregular disks in the system. The nanosheets eventually disappear completely and only Co_3O_4 nanospheres can be observed in the system (Fig. 4e1-2), after keeping the reaction at 200 °C for 5 h. The one-pot growth of Co_3O_4 granules in the approach is dramatically different in comparison to the fabrication of 3D Co_3O_4 nanostructures based on topotactic transformations, where Co-related precursors are first produced and then annealed at *ca*. 400 °C to produce hierarchical nanostructures with polycrystalline feature.[1i] The structures of the materials produced in the reaction further change into dendritic nanoparticles (Fig. S4-7) with polycrystalline nature and much lower yields, after keeping the reaction at 200 °C for 6 and 11 h, respectively.

Fig. 5a and Fig. S8 show the TEM images of a dendritic structure on the surface of a piece of nanosheet. The nanocuboids of the first generation (G1) split to produce multiple branches of the second generation (G2, highlighted with white arrows), and therefore form dendric structure. The HRTEM of the branches is composed of d-spacing of 0.23 nm corresponding to (222) facets. The nanocuboids grow along their <001> directions and exposed in {100} facets of cubic Co_3O_4. In addition, the dendric nanocube as shown in Fig. 4c2 is further illustrated in Fig. 5c. It can be observed that more than three generations of the nanocuboids crossly stack to form the dendric structure. The HRTEM image (Fig. 5d) the dendritic nanostructure shows that it consists of nanocuboids with d-spacing of 0.28 nm corresponding to (220) facets of cubic Co_3O_4. The results suggest the stepwise splitting growth of the dendric nanocubes, and further verify the single crystalline nature of the hierarchical superstructure. The nanocuboids grow step-by-step on the {100} facets of cubic Co_3O_4 to generate porous nanospheres through partially sharing their (100), (010) and (001) planes.

Based on the experimental observations, a stepwise splitting mechanism (Fig. 6) can be proposed to understand the formation of the porous and single crystalline Co_3O_4 nanospheres. AOT and cobalt ions first form 2D lamellar assemblies consisting of AOT double-layer and two Co^{2+} layers to form nanoreactors (S1). The Co^{2+} ions then hydrolyze to form Co_3O_4 to form nanosheets together with AOT assemblies (S2), after reacting at 200 °C for 2 h. After prolonging the reaction time to 3 h, the Co_3O_4 nanosheets start to convert into Co_3O_4 dendric nanocubes consisting of nanocuboids for the Ostwald ripening. Because the nucleation and growth of Co_3O_4 could simultaneously take place at multiple sites on the surfaces of the nanosheets and then form nanocuboids, 3D dendric nanocubes (S3) can be therefore constructed at the expense of Co_3O_4 nanosheets. Porous and single crystalline Co_3O_4 nanospheres exposed in {100} facets can be eventually produced by the stepwise splitting growth of nanocuboids (S4-5). During the formation of the Co_3O_4 nanospheres, AOT surfactant may have played three roles critical: (1) the first, constructing lamellar assemblies together with Co^{2+} ions as nanoreactors (Eq. 2-3); (2) the second, confining the fast growth of Co_3O_4 nanosheets; (3) the third, directing the growth of nanocuboids for selectively binding to the {100} facets of cubic Co_3O_4 on the surfaces of nanosheets to produce porous and single crystalline nanospheres. Due to Co_3O_4 can also be etched by NH_3 and AOT in the system (Eq. 4), the nanospheres change their morphology into dendritic particles after further reacting for longer time. It is worth to note that the 2D nanosheets also play a role critical in the formation of the Co_3O_4 nanospheres. Because the granules are in-situ generated on the surfaces of nanosheets, a flat and smooth facet can be produced on the surfaces of some nanospheres to form hemispheres.

$$Co^{2+} + 2AOT^{-} \rightarrow Co(AOT)_2 \quad (2)$$

$$Co(AOT)_2 + 6NH_3 \cdot H_2O \rightarrow Co(NH3)_6(AOT)_2 \quad (3)$$

$$3Co(NH_3)_6(AOT)_2 + 3H_2O + 1/2O_2 \Leftrightarrow Co_3O_4 + 12NH_3 + 6NH_4^{+} + 6AOT^{-1} \quad (4)$$

Using as-prepared nanospheres as electrode materials, we further made pseudocapacitors and investigated their charge storage performances. Fig. 7a shows cyclic voltammograms (CVs) of the pseudocapacitors recorded at different scan rates between 5 and 50 mV s^{-1} in 6 M KOH solution. All of the CV curves show obvious pseudocapacitance features consisting of a pairs of redox peaks. The peak currents of the CV curves increase as the scan rate increases, which suggest the good reversibility of the fast charge-discharge behaviours of the materials.

Fig. 7b shows the charge and discharge curves of the pseudocapacitors made with as-prepared materials, measured at different discharge current densities within the potential window of -0.07 – 0.33 V in 6 M KOH solution. The specific capacitances (Fig. 5c) of porous and single crystalline nanospheres evaluated

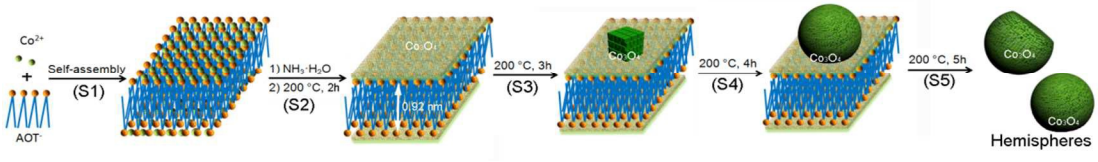

Fig. 6. Stepwise self-assembly growth of Co_3O_4 hemispheres.

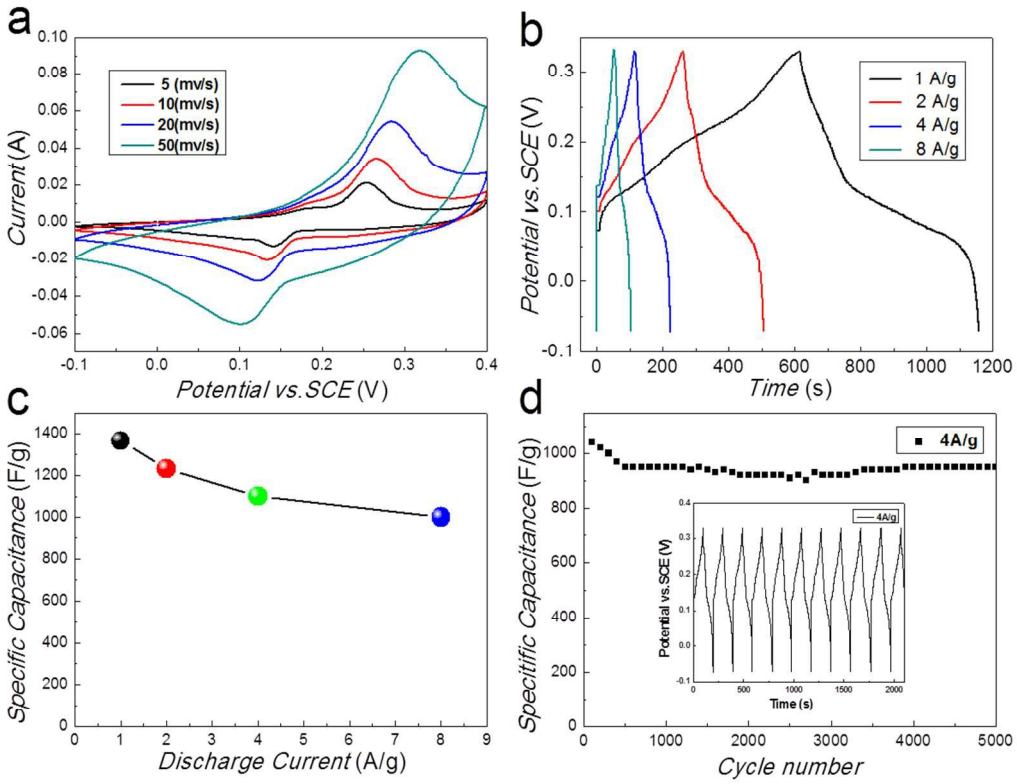

Fig. 7. a) CV curves of the electrode made with Co_3O_4 nanospheres in 6.0 M KOH at different scan rates. b) The charge-discharge curves of the supercapacitors made with Co_3O_4 nanospheres measured at different current densities. c) Average specific capacitance of the devices at various discharge current densities. d) Average specific capacitance versus cycle number of supercapacitors at a galvanostatic charge-discharge current density of 4 A g^{-1}, the insets show the galvanostatic charge-discharge curves of the device at a current density of 4 A g^{-1}.

from the discharge curves were 1350, 1230, 1100 and 1000 F g^{-1} at current densities of 1, 2, 4, and 8 A g^{-1}, respectively. The pseudocapacitors made with porous and single crystalline Co_3O_4 nanospheres exhibit more than 2 times higher ability in storing charges, compared to the devices (Fig. S9) fabricated with dendritic nanoparticles (Fig. S4-7) produced by prolonging the reaction time to more than 6 hours. The supercrystals with pores and single crystalline features also show much higher abilities in storing charges in comparison with single crystalline Co_3O_4 nanospheres grown around MWCNTs,[11h] 3D hierarchical Co_3O_4 twin-spheres[11] and 3D hierarchical Co_3O_4 nanoarchitectures consisting of nanowalls we reported previously.[11g] In addition, the devices made with porous and single crystalline Co_3O_4 nanospheres also exhibit much higher specific capacitances than those fabricated with Co_3O_4 nanoparticles,[12] hollow nanowire arrays,[1m] nanotubes[13] and mesoporous monolayer.[1f] The electrode materials show charge storage ability comparable to RuO_2 materials, which are of high costs and therefore prohibitive for most applications.[5,14] The porous and single crystalline features of the Co_3O_4 nanospheres could facilitate both high ion permeability and rapid electron transportation in the 3D hierarchical structures similar to porous and single crystalline TiO_2 nanospheres.[9]

While the specific capacitances of the devices also decrease as increasing the charge-discharge current density for the increase of the potential drop for the resistance of the nanoparticles and the relatively insufficient Faradic redox of the active material under higher charge-discharge current densities, the value of 1000 F g^{-1} at 8 A g^{-1} of the pseudocapacitors only decreases 25.9% (Fig. 5c) in comparison with its specific capacitance of 1350 F g^{-1} at 1 A g^{-1}. The low fading rate in the capacitance of materials at high galvanostatic current density indicates that the materials allow for the reaction taking place rapidly at high current densities, which can be attributed to the novel porous and single crystalline structure of as-prepared materials also.

Fig. 7d shows the cycling performance of the pseudocapacitors made with Co_3O_4 nanospheres at a current density of 4 A g^{-1} within the potential window of -0.07 – 0.33 V. After cycling for first 200 times, specific capacitance of the device first decreased from 1100 to 930 F g^{-1}, which could be resulted from the consumption of electrolyte secondary to irreversible reaction between the electrode materials and electrolyte. The capacitance of the device was stable after the initial drop. It was retained at 84.5% of 1100 F g^{-1}, after cycling for 5000 times. The inset in Fig. 7d presents the charge-discharge curves of the devices showing their high reversibility. The porous and single crystalline Co_3O_4 nanospheres are promising candidates for designing novel pseudocapacitors with excellent performances.

Conclusions

In summary, Co_3O_4 nanospheres with porous and single crystalline nature have been produced successfully on a large scale. It was found that the reaction time can dramatically affect the growth of Co_3O_4 superstructures in the nanoreactors constructed with AOT^- and Co^{2+} ions. The experimental observations strongly support a stepwise splitting mechanism proposed to understand the formation of the superstructures. The

pseudocapacitors made with the porous and single crystalline Co_3O_4 nanospheres exhibit excellent charge-storage performances. The superior electrochemical properties of the materials can be attributed to their superstructures with pores and single crystalline feature, which may significantly increase the rate of both ion diffusion and electron transportation. The approach described here shows four major advantages: the first, novel porous and single crystalline 3D Co_3O_4 supercrystals mainly exposed in {100} facets can be produced on a large scale; the second, the one-pot approach is much more convenient and efficient in synthesizing 3D nanoarchitectures, compared to the topotactic transformation; the third, the formation mechanism proposed could be applied to fabricate other functional materials; and the fourth, the supercrystals exhibit excellent capability in storing charges for their porous and single crystalline features. By choosing a suitable surfactant such as AOT, 3D hierarchical nanoarchitectures with novel microstructures can be fabricated successfully for energy storage.

Acknowledgements

The authors are grateful to the financial support from the National Natural Science Foundation of China (NSFC. 21071130 and 21371157), Outstanding Scholar Program of Henan Province (114200510012) and Key Program of Henan Province for Science and Technology (132102210424).

Notes and references

[a] *State Laboratory of Surface and Interface Science and Technology, Collaborative Innovation Center of Environmental Pollution Control and Ecological Restoration, Zhengzhou University of Light Industry, Zhengzhou 450001, China; Fax: 86-371-86609676; Tel: 86-371-86609676; E-mail: fengli@zzuli.edu.cn; lifeng696@yahoo.com*

[b] *State Key Laboratory of Coordination Chemistry, Nanjing University Nanjing 210093, Jiangsu, China*

[c] *American Advanced Nanotechnology, Houston, TX 77459, USA; E-mail: lifeng696@yahoo.com*

†Electronic Supplementary Information (ESI) available: TEM, HRTEM and FSEM images for this article are given via a link at the end of the document. See DOI: 10.1039/b000000x/

1 a) S. L. Xiong, C. Z. Yuan, M. F. Zhang, B. J. Xi, Y. T. Qian, *Chem.-Eur. J.* **2009**, *15*, 5320; b) C. Z. Yuan, L. Yang, L. R. Hou, L. F. Shen, F. Zhang, D. K. Li, X. G. Zhang, *J. Mater. Chem.* **2011**, *21*, 18183; c) X. Wang, A. Sumboja, E. Khoo, C. Y. Yan, P. S. Lee, *J. Phys. Chem. C* **2012**, *116*, 4930; d) X. M. Liu, Q. Long, C. H. Jiang, B. B. Zhan, C. Li, S. J. Liu, Q. Zhao, W. Huang, X. C. Dong, *Nanoscale* **2013**, *5*, 6525; e) H. W. Shim, A. H. Lim, J. C. Kim, E. Jang, S. D. Seo, G. H. Lee, T. D. Kim, D. W. Kim, *Sci Rep* **2013**, *3*, 2325; f) X. H. Xia, J. P. Tu, X. L. Wang, C. D. Gu, X. B. Zhao, *Chem. Commun.* **2011**, 47, 5786; g) C. Z. Yuan, L. Yang, L. R. Hou, L. F. Shen, X. G. Zhang, X. W. Lou, *Energy Environ. Sci.* **2012**, *5*, 7883; h) T. Zhu, J. S. Chen, X. W. Lou, *J. Mater. Chem.* **2010**, *20*, 7015; i) Y. H. Xiao, S. J. Liu, F. Li, A. Q. Zhang, J. H. Zhao, S. M. Fang, D. Z. Jia, *Adv. Funct. Mater.* **2012**, *22*, 4052; j) D. W. Wang, Q. H. Wang, T. M. Wang, *Inorg. Chem.* **2011**, *50*, 6482; k) F. L. Meng, Z. G. Fang, Z. X. Li, W. W. Xu, M. J. Wang, Y. P. Liu, J. Zhang, W. R. Wang, D. Y. Zhao, X. H. Guo, *J. Mater. Chem. A* **2013**, *1*, 7235; l) R. T. Wang, L. B. Kong, J. W. Lang, X. W. Wang, S. Q. Fan, Y. C. Luo, L. Kang, *J. Power Sources* **2012**, *217*, 358; m) B. Wang, T. Zhu, H. B. Wu, R. Xu, J. S. Chen, X. W. Lou, *Nanoscale* **2012**, *4*, 2145.

2 a) S. L. Xiong, J. S. Chen, X. W. Lou, H. C. Zeng, *Adv. Funct. Mater.* **2012**, *22*, 861; b) X. L. Xiao, X. F. Liu, H. Zhao, D. F. Chen, F. Z. Liu, J. H. Xiang, Z. B. Hu, Y. D. Li, *Adv. Mater.* **2012**, *24*, 5762; c) Y. Wang, H. Xia, L. Lu, J. Y. Lin, *ACS Nano* **2010**, *4*, 1425; d) L. Tian, H. L. Zou, J. X. Fu, X. F. Yang, Y. Wang, H. L. Guo, X. H. Fu, C. L. Liang, M. M. Wu, P. K. Shen, Q. M. Gao, *Adv. Funct. Mater.* **2010**, *20*, 617; e) N. Du, H. Zhang, B. Chen, J. B. Wu, X. Y. Ma, Z. H. Liu, Y. Q. Zhang, D. Yang, X. H. Huang, J. P. Tu, *Adv. Mater.* **2007**, *19*, 4505; f) X. W. Lou, D. Deng, J. Y. Lee, J. Feng, L. A. Archer, *Adv. Mater.* **2008**, *20*, 258; g) J. Y. Wang, N. L. Yang, H. J. Tang, Z. H. Dong, Q. Jin, M. Yang, D. Kisailus, H. J. Zhao, Z. Y. Tang, D. Wang, *Angew. Chem.-Int. Edit.* **2013**, *52*, 6417; h) L. Hu, N. Yan, Q. W. Chen, P. Zhang, H. Zhong, X. R. Zheng, Y. Li, X. Y. Hu, *Chem.-Eur. J.* **2012**, *18*, 8971; i) K. T. Nam, D. W. Kim, P. J. Yoo, C. Y. Chiang, N. Meethong, P. T. Hammond, Y. M. Chiang, A. M. Belcher, *Science* **2006**, *312*, 885; j) Y. G. Li, B. Tan, Y. Y. Wu, *Nano Lett.* **2008**, *8*, 265.

3 W. Y. Li, L. N. Xu, J. Chen, *Adv. Funct. Mater.* **2005**, *15*, 851.

4 a) L. H. Hu, Q. Peng, Y. D. Li, *J. Am. Chem. Soc.* **2008**, *130*, 16136; b) X. W. Xie, Y. Li, Z. Q. Liu, M. Haruta, W. J. Shen, *Nature* **2009**, *458*, 746; c) Y. Y. Liang, Y. G. Li, H. L. Wang, J. G. Zhou, J. Wang, T. Regier, H. J. Dai, *Nat. Mater.* **2011**, *10*, 780.

5 a) J. R. Miller, P. Simon, *Science* **2008**, *321*, 651; b) P. Simon, Y. Gogotsi, *Nat. Mater.* **2008**, *7*, 845.

6 C. C. Li, X. M. Yin, L. B. Chen, Q. H. Li, T. H. Wang, *Chem.-Eur. J.* **2010**, *16*, 5215.

7 H. Huang, W. J. Zhu, X. Y. Tao, Y. Xia, Z. Y. Yu, J. W. Fang, Y. P. Gan, W. K. Zhang, *ACS Appl. Mater. Interfaces* **2012**, *4*, 5974.

8 Y. G. Li, B. Tan, Y. Y. Wu, *J. Am. Chem. Soc.* **2006**, *128*, 14258.

9 N. N. Edward, J. W. Crossland, V. Sivaram, T. Leijtens, J. A. Alexander-Webber, H. J. Snaith, *Nature* **2013**, *495*, 215.

10 J. Chmiola, G. Yushin, Y. Gogotsi, C. Portet, P. Simon, P. L. Taberna, *Science* **2006**, *313*, 1760.

11 a) F. Li, M. Zhu, C. G. Liu, W. L. Zhou, J. B. Wiley, *J. Am. Chem. Soc.* **2006**, *128*, 13342; b) F. Li, J. B. He, W. L. L. Zhou, J. B. Wiley, *J. Am. Chem. Soc.* **2003**, *125*, 16166; c) F. Li, X. Badel, J. Linnros, J. B. Wiley, *J. Am. Chem. Soc.* **2005**, *127*, 3268; d) F. Li, Y. Ding, P. X. X. Gao, X. Q. Xin, Z. L. Wang, *Angew. Chem.-Int. Edit.* **2004**, *43*, 5238; e) F. Li, F. L. Gong, Y. H. Xiao, A. Q. Zhang, J. H. Zhao, S. M. Fang, D. Z. Jia, *ACS Nano* **2013**, *7*, 10482; f) Y. H. Xiao, A. Q. Zhang, S. J. Liu, J. H. Zhao, S. M. Fang, D. Z. Jia, F. Li, *J. Power Sources* **2012**, *219*, 140; g) Y. H. Xiao, S. J. Liu, S. M. Fang, D. Z. Jia, H. Q. Su, W. L. Zhou, J. B. Wiley, F. Li, *RSC Adv.* **2012**, *2*, 3496; h) Y. Xiao, A. Zhang, D. Jia, F. Li, *Mater. Res. Soc. Symp. Proc. 1497*, Boston, MA, **2013**.

12 M. B. Zheng, J. Cao, S. T. Liao, J. S. Liu, H. Q. Chen, Y. Zhao, W. J. Dai, G. B. Ji, J. M. Cao, J. Tao, *J. Phys. Chem. C* **2009**, *113*, 3887.

13 G. X. Tong, J. G. Guan, Q. J. Zhang, *Adv. Funct. Mater.* **2013**, *23*, 2406.

14 S. W. Lee, B. M. Gallant, H. R. Byon, P. T. Hammond, S. H. Yang, *Energy & Environ. Sci.* **2011**, *4*, 1972.